EXPERIMENTAL RESEARCH OF THERMAL-FLOW
AND VIBRATION CHARACTERISTICS OF A 1 KW ORC MICROTURBINE

Tomasz Z. KACZMARCZYK[*] , Grzegorz ŻYWICA[*]

*Institute of Fluid-Flow Machinery, Polish Academy of Sciences, Department of Turbine Dynamics and Diagnostics,
Fiszera 14, 80-231 Gdansk, Poland

tkaczmarczyk@imp.gda.pl, gzywica@imp.gda.pl

Abstract: This paper discusses the experimental research findings on a high-speed microturbine in an ORC system using the low-boiling fluid HFE-7100. The microturbine prototype features a hermetic design and was developed using oil-free technology, incorporating gas bearings powered by a low-boiling fluid. One of the main objectives of the study was to determine the thermodynamic parameter ranges within which the microturbogenerator could operate correctly. Tests of the microturbine were conducted within a rotational speed range of 10,000 rpm to approximately 75,000 rpm, with receiver loads ranging from 200 W_e to 2,000 W_e. The power of the heat source and the flow rate of the HFE-7100 working fluid ranged from 12 to 20 kW_t and 30 to 60 g/s, respectively. The chosen range of heat source power was deliberate and simulated the actual operating conditions of domestic boilers. In addition to measurements of thermal, flow, and energy parameters, vibration measurements of the turbogenerator were carried out to assess the dynamic state of the machine. The study found that for each power level of the heat source, the optimum generator load was determined at which the electrical output of the system reached its maximum. The work includes the electrical and dynamic characteristics of the high-speed microturbogenerator.

Key words: microturbine, resistive load, ORC system, HFE-7100, experimental research, microturbine dynamics

1. INTRODUCTION

Respect for energy resource [1] is associated with the application of new energy technologies [2] that are environmentally friendly [3] and enable cooperation with renewable energy sources (RES) [4]. Organic Rankine cycle (ORC) systems [5], which can, for example, be powered by waste heat [6], fit into this idea. ORC systems can also work with air storage systems [7], nuclear power engineering systems [8], trilateral flash cycles (TFCs) [9], organic Rankine cycle–vapour compression cycle (ORC-VCC) systems [10], thermal systems [11], or direct-fired hot water boilers [12]. Hence, research is continually being carried out [13] on ORC systems [14] and their subassemblies [15, 16], including circulating pumps [17]. ORC systems use volume expanders [18, 19] and flow expanders [20, 21, 22]. Due to their design, single- or multi-stage turbines [23] are built to operate with partial admission of the working fluid [24, 25]. To improve the efficiency of turbine sets, research [26] and optimisation work are being carried out [27]. In ORC systems, both scroll [28] and vane [29] expanders are used as volume expanders.

It should be noted that working fluids [30] have a fundamental impact on the cycle's efficiency, and in ORC systems they are also the subject of analyses and studies [31]. Similarly, expander tests aim to determine the mechanical and/or electrical performance [32]. For example, Sun et al. [33] carried out studies on an axial microturbine in an ORC system, using R1233zde fluid. The tests show that, at a rotational speed of approximately 8,000 rpm, the microturbine achieved a power output of 812 W and an efficiency of 36%. In contrast, the cycle's maximum thermal efficiency was 2.15%.

According to a study by Kaczmarczyk et al. [34], a scroll expander powered by HFE-7100 fluid achieved an electrical output of approximately 980 W. In contrast, the expander efficiency and the cycle's thermal efficiency were 49.3% and approximately 3%, respectively. This means that as the power of ORC systems increases, both the efficiency of the expansion units and the thermal efficiency of the cycle also increase. This is also confirmed by the study by Sun et al. [35], which was conducted on a scroll expander in an ORC system using R245fa fluid. These results show that, at a power output of approximately 1,800 W, the thermal efficiency was approximately 6.4%.

This paper presents the research findings of a prototype microturbogenerator with a rated power of 1 kW. The research was conducted on an ORC microsystem using the low-boiling medium HFE-7100, under varying heat source power levels, working medium flow rates, and microturbine generator loads. The aim of the study was to determine the effect of the microturbine generator load on the electrical power output of the ORC system, the isentropic efficiency of the microturbine, the ORC efficiency, and the Carnot efficiency. The study shows that the maximum electrical output of the ORC system, approximately 625 W_e, was achieved at a heat source power of 18 kW_t and the highest flow rate of HFE-7100, 60 g/s. In contrast, the maximum isentropic efficiency of the microturbine, approximately 70%, was achieved at a heat source power of 14 kW_t and the lowest flow rate of the working fluid, 30 g/s. It was determined that the maximum efficiency of the ORC system, approximately 4.0%, was achieved at a heat source power of 14 kW_t and an HFE-7100 flow rate of 60 g/s. In contrast, a maximum Carnot efficiency of 45.7% was achieved at an HFE-7100 flow rate of 50 g/s and a heat source power of 20 kW_t.

Tomasz Z. Kaczmarczyk, Grzegorz Żywica
Experimental Research of Thermal-Flow and Vibration Characteristics of a 1 Kw ORC Microturbine

DOI: 10.65731/ama/2026-0015

Vibration measurements showed that the microturbine operated correctly across the range of rotational speeds tested and at the preset thermal and electrical loads. It was determined that the maximum vibration velocity recorded on the microturbine casing was 0.418 mm/s, occurring at 43,200 rpm.

2. TEST RIG

Fig. 1 shows a diagram of the test rig. The ORC system used a prototype two-module induction electric flow heater with a rated power of 2×24 kW$_e$ as the heat source, simulating a low-temperature heat source. The power of the heat source could be adjusted in increments of 0.1 kW$_e$. In contrast, using a PID controller, the temperature of the thermal oil could be regulated from ambient to 400 °C in 1 °C increments. The heat carrier was Shell Thermia B thermal oil, which transferred heat to the working medium in the evaporator. The low-boiling fluid HFE-7100 was used as the working medium, and its selected properties are listed in Table 1. After being heated in the evaporator, the working medium was directed to the regenerator via a bypass and then to the condenser. Heat from the condenser was dissipated in a fan cooler with a rated power of 50 kWt, in which an ethylene glycol solution was used as the coolant.
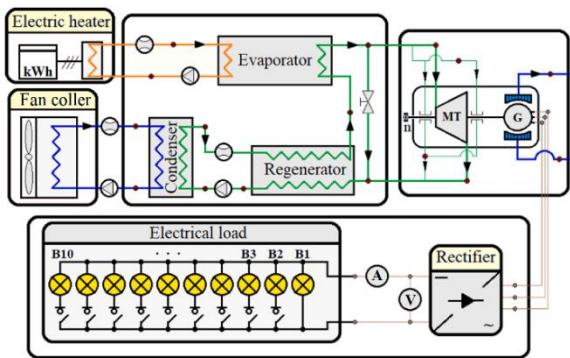

Fig. 1. Test rig diagram: A – ammeter, V – voltmeter, MT – microturbine, G – generator, B – bulb

Control of the flow rates of the working media (thermal oil, HFE-7100, and glycol solution) was realised by means of frequency converters mounted on the drives of the circulating pumps.

Tab. 1. Properties of HFE-7100 fluid at 25 °C

Property	Value	Unit
Molecular weight	250	g/mol
Boiling point	61	°C
Critical temperature	195	°C
Critical pressure	2.23	MPa
Liquid density	1,510	kg/m^3
Surface tension	13.6	mN/m
Dynamic viscosity	0.61	mPa s
Heat of vaporisation	112	kJ/kg
Vapour pressure	27.0	kPa
Coefficient of expansion	0.0018	1/K
Kinematic viscosity	0.38	cSt
Absolute viscosity	0.58	cP
Specific heat	1,183	J/kg K
Thermal conductivity	0.069	W/m K

After liquefaction, the HFE-7100 medium was directed into a tank and then, by means of a pump, to the regenerator and evaporator, respectively.

The working medium was circulated within the cycle until the appropriate vapour pressure was reached at the preset flow rate. Once the appropriate operating parameters had been achieved, the HFE-7100 medium was directed to the blade system of the microturbogenerator. The three-phase synchronous generator of the microturbogenerator was cooled using mains water. The generator was connected to a prototype AC/DC rectifier circuit. The load on the microturbogenerator's generator consisted of ten DC bulbs, each rated at 200 W$_e$ (Fig. 1). Load control of the generator was achieved by means of disconnectors (switches) fitted to each bulb. The minimum load required to prevent the microturbine generator from overspeeding was a single bulb.

2.1. Measuring apparatus and measurement error

A list of the measuring apparatus and sensors installed in the working medium cycle is provided in Table 2. Pressure transducers with maximum operating pressures of 16 bar and 10 bar were fitted to the microturbine inlet and outlet, respectively.

Tab. 2. Measuring apparatus and sensors in the HFE-7100 cycle

Instrument type/model (Manufacturer)	Range	Accuracy
Class 1 K-type thermocouple with a diameter of 0.5 mm (Czaki Thermo-Product)	-40 °C – 600 °C	± 0.0040·|t| [°C]
Pressure transducer, type NPXA, Class 0.1 (Peltron)	0 – 16 bar(a)	± 0.1% MR
Analogue manometer, Class 1.0 (Wika)	0 – 16 bar	± 0.16 bar MV
Pressure transducer, type NPXA, Class 0.1 (Peltron)	0 – 10 bar(a)	± 0.1% MV
Coriolis mass flowmeter, model Sitrans FC, type Mass 2100 (Siemens)	0 – 5,600 kg/h	± 0.1% MV (>50% MR)
Rotational speed measurement system with Garrett's inductive sensor (prototype)	6 – 80 krpm	± 2.5% MV
System for measuring current and voltage at the rectifier output (prototype)	0 – 10 A (DC)	± 1.5% MR
	0 – 400 V(DC)	± 1.0% MV
Two-module electric induction heater with a rated power of 2×24 kW$_e$ (prototype)	0 – 2 × 24 kW$_e$	± 1% MR
	-100 °C – 450 °C	± [0.15+0.002 t][*)
MV – measurement value, MR – measurement range, *) according to IEC 60751		

Table 2 shows that, for a minimum heat source power of 12 kW$_t$, the measurement uncertainty was ±3.0%, and for a maximum heat source power of 20 kW$_t$, it was approximately ±1.8%. Based on the manufacturer's data for the Coriolis flowmeter, the

uncertainty in measuring the working medium flow rate over the range of 30–60 g/s was calculated to be ±0.5 g/s.

In contrast, the combined uncertainty of the electrical power at the output of the AC/DC converter system of the ORC system was calculated using the quadratic error propagation rule, according to the following relationship:

$$\delta N_e = \sqrt{\left(\left|\frac{\delta N_e}{\delta u}\right|\delta u\right)^2 + \left(\left|\frac{\delta N_e}{\delta i}\right|\delta i\right)^2} \tag{1}$$

As calculated from equation (1), the uncertainty in the electrical power at the output of the ORC system was ±1.8% MV.

2.2. High-speed microturbogenerator

A photograph of the microturbogenerator, with a rated power of 1 kW$_e$, mounted on the test rig, is shown in Fig. 2. The microturbogenerator has a hermetic design, with a single-stage axial-flow microturbine, a high-speed generator, and gas bearings—supplied with the working medium—mounted within a single casing. The microturbine and generator were mounted on a single shaft.

Fig. 2. Prototype microturbogenerator installed on the test rig

The three-phase 1.7 kW$_e$ permanent magnet synchronous generator used had a maximum rotational speed of 120,000 rpm. The stator of the generator was of insulation class F, with a maximum operating temperature of 155 °C. In contrast, the maximum temperature of the working medium in transient states can exceed 195 °C. Hence, the microturbogenerator design incorporates a shell-and-tube heat exchanger supplied with tap water.

In contrast, the microturbine was designed with partial admission due to the high operating pressure required in the ORC system and the low flow rate of the HFE-7100 working medium. The microturbine had a partial admission ratio of 29%. The rotor disc of the microturbine had an outer diameter of 36.2 mm and 35 blades, each with a height of 3.3 mm. In contrast, the stator of the microturbine had three blades, each with a height of 2.9 mm.

2.3. Research procedure

The research procedure is shown in Fig. 3. In the first stage of the work, the heat source power was set, and the thermal oil cycle was started. The required working medium flow rate was then preset, and both the working medium cycle and the cooling system

(condenser heat removal system) were activated. During the heating and evaporation process, the working medium was directed through a bypass to the microturbine. The cooling system for the microturbogenerator's generator was then started. Before start-up, the generator was connected to a load with a total rated power of 2,000 W for all electrical receivers (bulbs) (Fig. 3). Once stable operation of the ORC system had been achieved at a constant heat source power and flow rate, the HFE-7100 medium was directed to the bearing system (with the valves supplying the microturbine blade system closed), and the microturbine casing was heated.
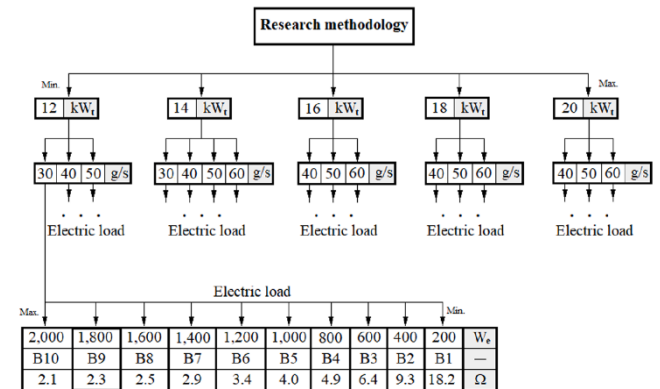

Fig. 3. Research procedure used for the prototype microturbogenerator

Once the casing was heated, the blade system was supplied, while the vibration level and rotational speed of the microturbogenerator were monitored. Once it had been determined that the dynamic state of the machine and the thermodynamic parameters of the working medium were correct, the actual tests commenced. With a constant, preset heat source power level and working fluid flow rate, the generator loads were reduced in accordance with the research procedure shown in Fig. 3.

2.4. Method

The electrical power at the output of the ORC system, that is, after the AC/DC frequency converter, was calculated using the following relationship:

$$N_e = U \cdot I \tag{2}$$

where: U – voltage [V]; I – current [A].

The isentropic efficiency of the microturbine was calculated using the following relationship:

$$\eta_{is} = \frac{h_1 - h_2}{h_1 - h_{2s}} \tag{3}$$

where:

h_1 – enthalpy of the working fluid at the microturbine inlet [J/kg],
h_2 – enthalpy of the working fluid at the microturbine outlet [J/kg],
h_{2s} – enthalpy of the working fluid at the outlet of the scroll expander under isentropic expansion [J/kg].

The Carnot efficiency was calculated using the following relationship:

$$\eta_{Car} = 1 - \frac{T_{min}}{T_{max}} \tag{4}$$

where:

T_{min} – minimum temperature of the working medium (after the

Tomasz Z. Kaczmarczyk, Grzegorz Żywica
Experimental Research of Thermal-Flow and Vibration Characteristics of a 1 Kw ORC Microturbine

DOI: 10.65731/ama/2026-0015

condenser) [K],

T_{max} – maximum temperature of the HFE-7100 medium (after the evaporator) [K].

The efficiency of the ORC system was calculated using the following relationship:

$$\eta_{ORC} = \frac{N_e}{N_S} \tag{5}$$

where:

N_e – electrical power output of the ORC system [W],

N_S – heat source power [W].

3. RESEARCH RESULTS AND DISCUSSION

The research results, showing the effect of generator load on the electrical power output, Carnot efficiency, isentropic efficiency of the microturbine, and the overall efficiency of the ORC system for different thermal power levels of the heat source and preset constant flow rates of the HFE-7100 working medium, are presented below. The research on the microturbogenerator was conducted for five predetermined heat source power levels (Fig. 3). For a heat source with a power of 12 kWe, the average thermal oil temperatures measured at the outlet of the electric heater, for HFE-7100 flow rates of 30 g/s, 40 g/s, and 50 g/s, were 181 °C, 181 °C, and 166 °C, respectively. In contrast, for a heat source with a power of 14 kWe, the average thermal oil temperatures for working fluid flow rates of 30 g/s, 40 g/s, 50 g/s, and 60 g/s were 197 °C, 205 °C, 197 °C, and 178 °C, respectively. When the heat source power was 16 kWe, the average thermal oil temperatures at the heater outlet for low-boiling medium flow rates of 40 g/s, 50 g/s, and 60 g/s were 193 °C, 200 °C, and 191 °C, respectively. For a heat source with a power of 18 kWe, the average thermal oil temperatures at the heater outlet for HFE-7100 flow rates of 40 g/s, 50 g/s, and 60 g/s were 221 °C, 210 °C, and 179 °C, respectively. In contrast, for a maximum power of 20 kWe, the average thermal oil temperatures measured at the outlet of the electric oil heater for HFE-7100 flow rates of 40 g/s, 50 g/s, and 60 g/s were 216 °C, 235 °C, and 231 °C, respectively.

3.1. Effect of generator load on electrical power

Example characteristics illustrating the effect of generator load on the electrical power output of the ORC system at heat source powers of 12 kWt, 16 kWt, and 20 kWt are presented in Figs. 4–6. The study shows that, irrespective of the heat source power, the electrical power output of the ORC system increased with the flow rate of the HFE-7100 medium. It was observed that, at a constant heat source power and maximum electrical output, the optimum load resistance decreased as the HFE-7100 medium flow rate increased, with the optimum load line (L) sloping to the left.

For example, for a heat source power of 12 kWt, the maximum electrical powers for working medium flow rates of 30 g/s, 40 g/s, and 50 g/s were 210 We, 335 We, and 415 We, respectively. These were obtained with load resistances (i.e. the resistances of the electrical receivers) of 4.5 Ω, 3.5 Ω, and 2.8 Ω, respectively (Table 3). In contrast, for the maximum heat source power, the maximum electrical powers were 350 We, 490 We, and 625 We, respectively, obtained at loads of 4.2 Ω, 3.3 Ω, and 2.6 Ω.

It was observed that, irrespective of the power level of the heat source, the relative increase in electrical power, ΔNe, decreased as the flow rate of the working medium increased.
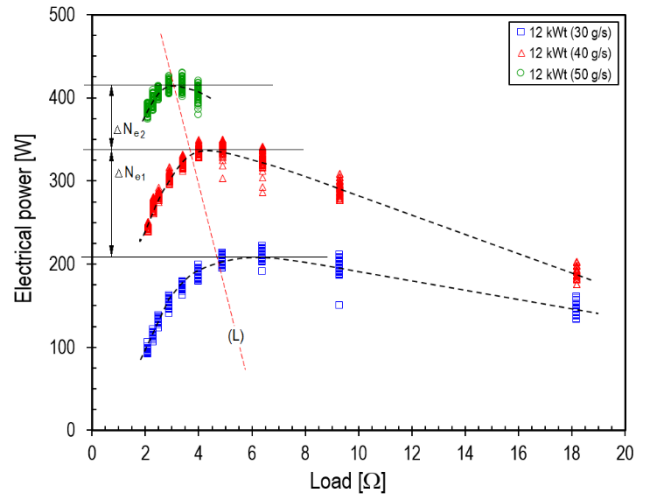

Fig. 4. Effect of generator load on the electrical power of the ORC system at a heat source power of *12 kWt: L* – line of optimal load
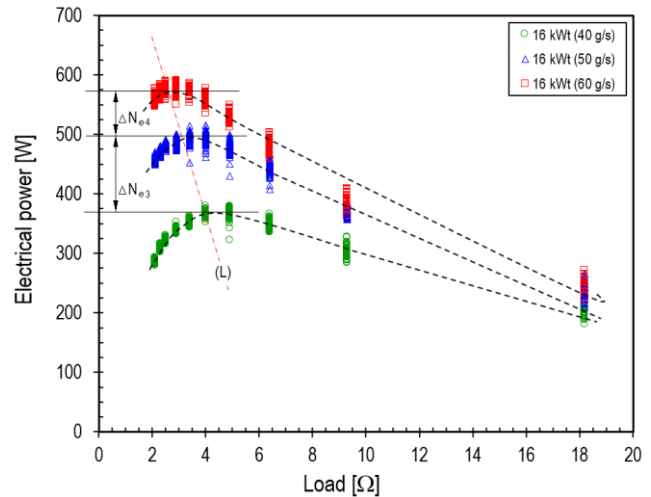

Fig. 5. Effect of generator load on the electrical power of the ORC system at a heat source power of *16 kWt*
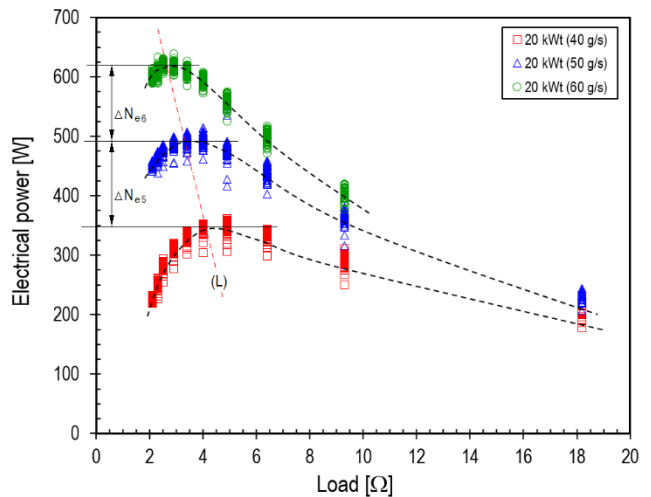

Fig. 6. Effect of generator load on the electrical power of the ORC system at a heat source power of *20 kWt*

For a thermal power of 12 kW$_t$, the electrical power increases, ΔN_{e1} and ΔN_{e2}, were approximately 125 W$_e$ and 80 W$_e$, respectively. In contrast, for heat source powers of 16 kW$_t$ (Fig. 5) and 20 kW$_t$ (Fig. 6), the increases in electrical power, ΔN_{e3}, ΔN_{e4}, ΔN_{e5}, and ΔN_{e6}, were 130 W$_e$, 75 W$_e$, 140 W$_e$, and 135 W$_e$, respectively. The maximum electrical power output of the ORC system, approximately 625 W$_e$, was achieved at a heat source power of 18 kW$_t$. At a heat source power of 20 kW$_t$, the electrical output was lower than at 18 kW$_t$ (Table 3).

From the above, it can be concluded, firstly, that for a given thermal power of the heat source, there exists an optimum value of the working fluid flow rate at which the electrical power output of the ORC system is maximised. Secondly, for each level of thermal power and preset working fluid flow rate, there is an optimum generator load at which the electrical power output of the ORC system is maximised.

Tab. 3. Electrical power output maxima of the ORC system

m [g/s]	30	40	50	60	N$_s$ [W]
N$_e$ [W]	210	335	415	–	12,000
L [Ω]	4.5	3.5	2.8	–	12,000
N$_e$ [W]	200	350	455	545	14,000
L [Ω]	5.1	3.8	3.5	2.0	14,000
N$_e$ [W]	–	370	500	575	16,000
L [Ω]	–	4.0	3.1	2.6	16,000
N$_e$ [W]	–	350	515	625	18,000
L [Ω]	–	4.0	3.5	2.6	18,000
N$_e$ [W]	–	350	490	620	20,000
L [Ω]	–	4.2	3.3	2.6	20,000

Thirdly, it was determined that, for heat source powers in the range of 12–20 kW$_t$ and HFE-7100 flow rates between 30 and 60 g/s, the optimum generator load at which the electrical power output of the ORC system was maximised lay within the range of 2.6–5.1 Ω.

3.2. Effect of load on isentropic efficiency

Selected characteristics illustrating the effect of generator load on the isentropic efficiency of the microturbine are shown in Figs. 7–9.
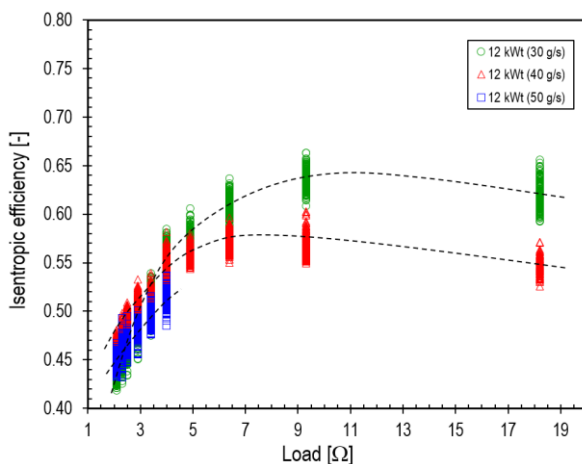

Fig. 7. Effect of generator load on the microturbine's isentropic efficiency at a heat source power of *12 kW$_t$*

It was determined that, regardless of the heat source power, the isentropic efficiency of the microturbine decreased with increasing flow rate of the HFE-7100 medium.The study shows that, at constant heat source power, the optimum load resistance corresponding to the maximum electrical power increased as the flow rate of the HFE-7100 medium increased. For a heat source power of 12 kW$_t$ and working medium flow rates of 30 g/s, 40 g/s, and 50 g/s, the maximum isentropic efficiencies of the microturbine were 64%, 58%, and 51%, respectively, achieved at loads of 11.0 Ω, 7.5 Ω, and 4.0 Ω, respectively (Table 4).

The study shows that, at a heat source power of 14 kW$_t$, the microturbine achieved a maximum isentropic efficiency of approximately 70%.
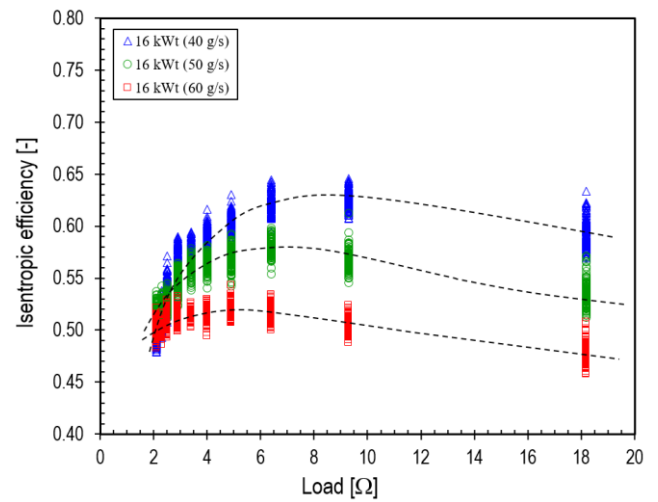

Fig. 8. Effect of generator load on the microturbine's isentropic efficiency at a heat source power of *16 kW$_t$*
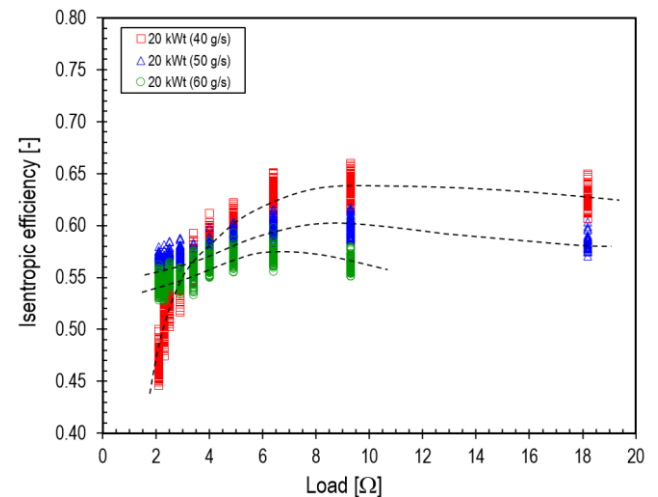

Fig. 9. Effect of generator load on the microturbine's isentropic efficiency at a heat source power of *20 kW$_t$*

From the above, it follows, firstly, that for a given thermal power of the heat source, there is an optimum value of the working medium flow rate at which the isentropic efficiency of the microturbine is maximised.

Secondly, for each thermal power level and preset working medium flow rate, there is an optimum generator load at which the isentropic efficiency of the microturbine is maximised.

Tomasz Z. Kaczmarczyk, Grzegorz Żywica
Experimental Research of Thermal-Flow and Vibration Characteristics of a 1 Kw ORC Microturbine

DOI: 10.65731/ama/2026-0015

Tab. 4. Isentropic efficiency maxima of the microturbine

m [g/s]	30	40	50	60	N_s [W]
η_{is} [-]	0.64	0.58	0.51	–	12,000
L [Ω]	11.0	7.5	4.0	–	12,000
η_{is} [-]	0.70	0.60	0.58	0.50	14,000
L [Ω]	10.5	6.5	3.8	3.5	14,000
η_{is} [-]	–	0.63	0.58	0.52	16,000
L [Ω]	–	8.5	7.0	5.5	16,000
η_{is} [-]	–	0.68	0.63	0.58	18,000
L [Ω]	–	8.5	6.7	7.5	18,000
η_{is} [-]	–	0.64	0.61	0.58	20,000
L [Ω]	–	10.0	8.5	6.7	20,000

Thirdly, it was determined that, for a heat source power in the range of 12–20 kW$_t$ and an HFE-7100 flow rate between 30 and 60 g/s, the maximum isentropic efficiency of the microturbine ranged from 50% to 70%, achieved at a load between 3.5 and 10.5 Ω.

3.3. Effect of load on Carnot efficiency

Fig. 10 shows that, at a working medium flow rate of 30 g/s, the Carnot efficiency increased as the load resistance of the microturbine generator rose from 2.1 Ω to 9.3 Ω.
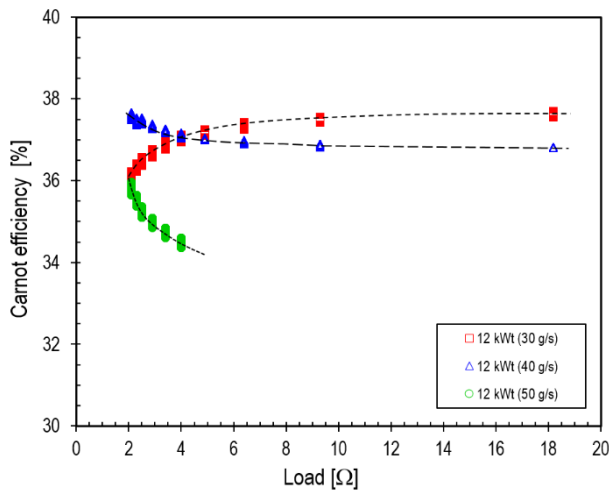

Fig. 10. Effect of generator load on Carnot efficiency at a heat source power of *12 kW$_t$*

The opposite trend was observed at HFE-7100 flow rates of 40 g/s and 50 g/s. In contrast, above a resistance of 9.3 Ω, regardless of the working medium flow rate and the heat source power, the Carnot efficiency remained practically constant, as shown in Figs. 11 and 12. For a heat source power of 12 kW$_t$, a maximum Carnot efficiency of approximately 37.5% was achieved at an HFE-7100 flow rate of 30 g/s (Table 5).

In contrast, for heat source powers in the range of 12–20 kW$_t$, a maximum Carnot efficiency of approximately 45.7% (Table 5) was obtained at an HFE-7100 flow rate of 50 g/s and a heat source power of 20 kW$_t$. The optimum load on the microturbine generator, for flow rates in the range of 30–60 g/s and heat source powers between 12 and 20 kW$_t$, was between 2.1 Ω and 9.3 Ω. In addition, the study shows that, for each thermal power level of the heat

source and a working fluid flow rate in the range of 30–60 g/s, the maximum difference between the Carnot efficiency maxima does not exceed 1.8 percentage points, this occurring at a heat source power of 14 kW$_t$.
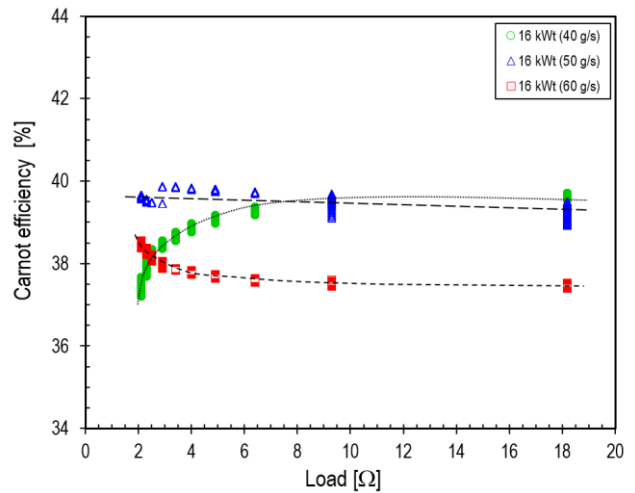

Fig. 11. Effect of generator load on Carnot efficiency at a heat source power of *16 kW$_t$*

In other cases, the maximum difference between the efficiency maxima did not exceed 0.7%.
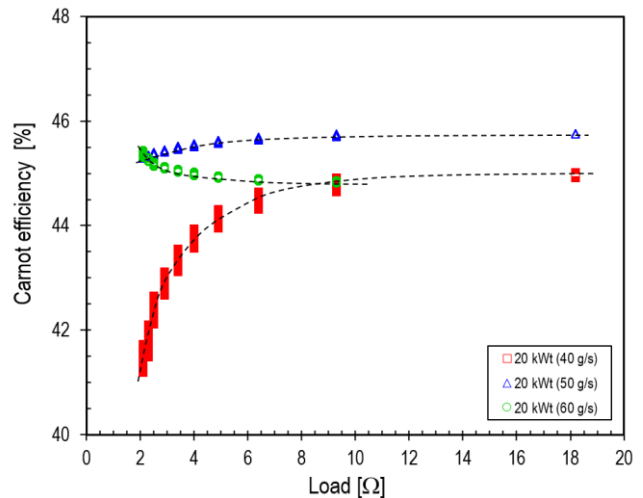

Fig. 12. Effect of generator load on Carnot efficiency at a heat source power of *20 kW$_t$*

Tab. 5. Carnot efficiency maxima of the HFE-7100 cycle

m [g/s]	30	40	50	60	N_s [W]
η_{Car} [%]	37.5	36.7	36.1	–	12,000
L [Ω]	9.3	2.1	2.1	–	12,000
η_{Car} [%]	40.0	40.2	40.0	37.7	14,000
L [Ω]	9.3	9.3	2.1	2.1	14,000
η_{Car} [%]	–	39.0	39.9	38.6	16,000
L [Ω]	–	9.3	2.1	2.1	16,000
η_{Car} [%]	–	41.5	42.5	41.8	18,000
L [Ω]	–	2.1	9.3	2.1	18,000
η_{Car} [%]	–	45.0	45.7	45.5	20,000
L [Ω]	–	9.3	9.3	2.1	20,000

For example, for a heat source power of 12 kW$_t$, the average maximum Carnot efficiency was 36.8 ± 0.7%. In contrast, for heat source powers of 16 kW$_t$, 18 kW$_t$, and 20 kW$_t$, the average maximum Carnot efficiencies were 39.2 ± 0.7%, 41.9 ± 0.6%, and 45.4 ± 0.4%, respectively.

The study shows that, for heat source powers in the range of 12–20 kW$_t$ and HFE-7100 flow rates between 30 and 60 g/s, the Carnot efficiency ranged from 36.1% to 45.7% (Table 5).

3.4. Effect of load on ORC system efficiency

Example characteristics illustrating the effect of generator load on the ORC system efficiency for heat source powers of 12 kW$_t$, 16 kW$_t$, and 20 kW$_t$ are shown in Figs. 13–15, respectively. It was determined that, irrespective of the heat source power, the efficiency of the ORC system increased as the flow rate of the working medium increased. It was found that, for a preset heat source power and maximum ORC system efficiencies, the optimum load resistance decreased as the HFE-7100 medium flow rate increased, with the load line (L) sloping to the left.
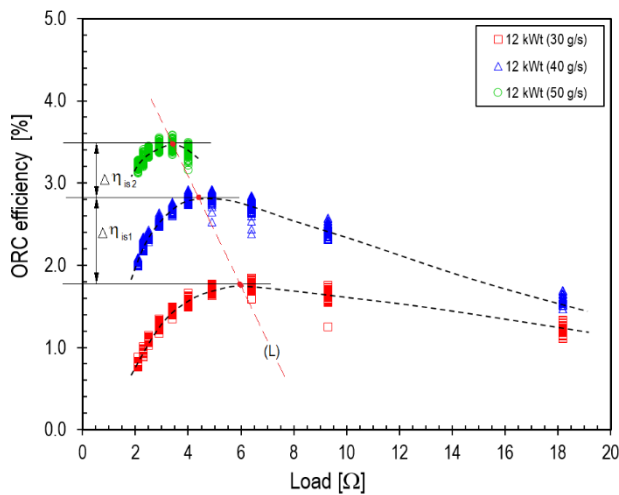

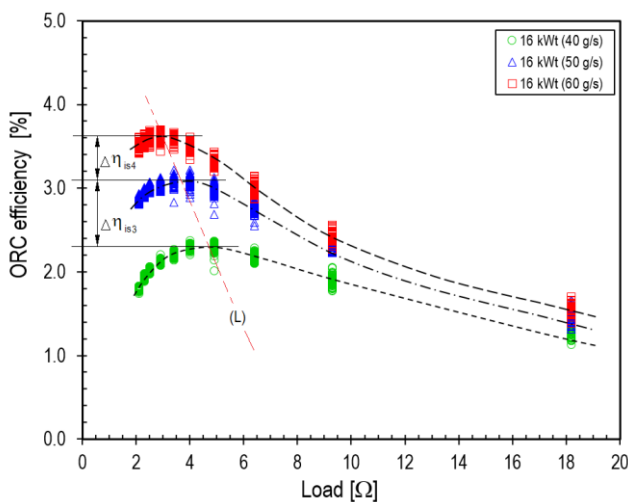**Fig. 13.** Effect of generator load on ORC system efficiency at a heat source power of *12 kW$_t$*

Fig. 14. Effect of generator load on ORC system efficiency at a heat source power of *16 kW$_t$*

For example, at a heat source power of 12 kW$_t$, the efficiency maxima at working medium flow rates of 30 g/s, 40 g/s, and 50 g/s were 1.8%, 2.8%, and 3.5%, respectively, which were obtained with load resistances of 6.0 Ω, 4.5 Ω, and 3.5 Ω, respectively (Table 6). In contrast, at heat source powers of 16 kW$_t$ and 20 kW$_t$, and HFE-7100 flow rates of 40 g/s, 50 g/s, and 60 g/s, the efficiencies were 2.3%, 3.1%, and 3.6% for 16 kW$_t$, and 1.8%, 2.5%, and 3.1% for 20 kW$_t$, respectively.

The optimum generator load values for the above ORC system efficiency maxima were 4.3 Ω, 3.5 Ω, and 3.0 Ω for 16 kW$_t$, and 4.5 Ω, 3.5 Ω, and 2.5 Ω for 20 kW$_t$, respectively. From the research conducted, it can be seen that the maximum ORC system efficiency of approximately 4.0% was achieved for a heat source power of 14 kW$_t$ at an HFE-7100 flow rate of 60 g/s.

The study shows that, irrespective of the heat source power level, the increase in isentropic efficiency of the microturbine ($\Delta\eta_{is}$) decreased with increasing flow rate of the working medium. For example, at a heat source power of 12 kW$_t$, the increments in isentropic efficiency, $\Delta\eta_{e1}$ and $\Delta\eta_{e2}$, were 1.0% and 0.7%, respectively. For a heat source power of 16 kW$_t$ (Fig. 14), the increases in efficiency, $\Delta\eta_{e3}$ and $\Delta\eta_{e4}$, were 0.8% and 0.5%, respectively. In contrast, for a heat source power of 20 kW$_t$ (Fig. 15), the increases in efficiency, $\Delta\eta_{e5}$ and $\Delta\eta_{e6}$, were 0.7% and 0.6%, respectively.
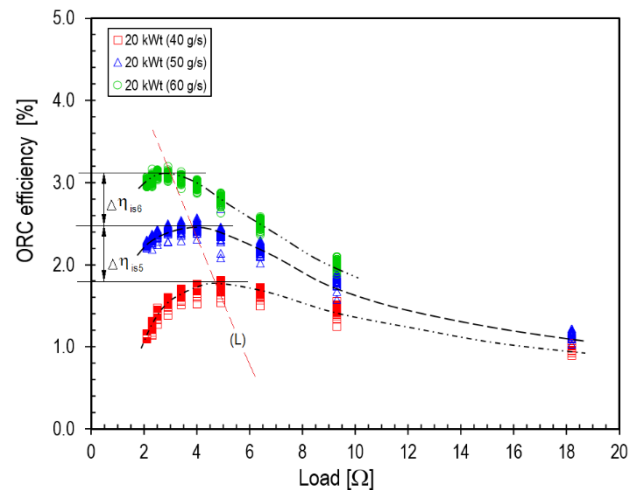

Fig. 15. Effect of generator load on ORC system efficiency at a heat source power of *20 kW$_t$*

It is worth noting that, at the preset HFE-7100 flow rates, the increases in efficiency decreased as the heat source power increased.

Tab. 6. ORC efficiency maxima

m [g/s]	30	40	50	60	N$_s$ [W]
η_{ORC} [%]	1.8	2.8	3.5	–	12,000
L [Ω]	6.0	4.5	3.5	–	12,000
η_{ORC} [%]	1.5	2.6	3.3	4.0	14,000
L [Ω]	6.1	4.5	3.2	2.2	14,000
η_{ORC} [%]	–	2.3	3.1	3.6	16,000
L [Ω]	–	4.3	3.5	3.0	16,000
η_{ORC} [%]	–	1.9	2.8	3.4	18,000
L [Ω]	–	4.5	3.5	2.8	18,000
η_{ORC} [%]	–	1.8	2.5	3.1	20,000
L [Ω]	–	4.5	3.5	2.5	20,000

Tomasz Z. Kaczmarczyk, Grzegorz Żywica
Experimental Research of Thermal-Flow and Vibration Characteristics of a 1 Kw ORC Microturbine

DOI: 10.65731/ama/2026-0015

Furthermore, it was observed that, for heat source powers of 20 kW$_t$ and 18 kW$_t$, the ORC system efficiencies obtained were lower than those achieved at a heat source power of 16 kW$_t$ (Table 6). This indicates that there is an optimum value of heat source power at which the efficiency of the ORC system will be maximised. Hence, it can be said that, for a preset thermal power of the heat source, there is an optimum value of the working medium flow rate at which the efficiency of the ORC system will be maximised. In addition, for each thermal power level and preset working medium flow rate, there is an optimum value of generator load at which the efficiency of the ORC system will be maximised.

To summarise, it can be concluded that for a heat source power in the range of 12–20 kW$_t$ and an HFE-7100 flow rate in the range of 30–60 g/s, the optimum generator load (Table 6) at which the ORC system efficiency was maximised lay within the range of 2.2–6.1 Ω.

3.5. Vibration measurements of the microturbine

Vibration measurements of fluid-flow machines enable an assessment of their impact on the immediate environment and are crucial for determining their potential applications. Excessive vibration levels, and the associated noise, preclude the use of certain machines in domestic environments. In addition, detailed vibration analysis complements thermal and flow measurement results and enables the early detection of malfunctions or damage that may occur during operation. This is particularly important for high-speed machines, such as microturbines.

To assess the dynamic state of the microturbine during the studies described earlier, its vibration level was continuously monitored. Vibrations were measured on the machine casing in the vicinity of the bearing node situated between the generator and the blade system. High-temperature single-axis accelerometers, connected to an MBJ Diamond 401AXT portable vibration analyser, were used to measure vibrations. The accelerometers were mounted on the microturbine casing using magnetic feet positioned on stands made of ferromagnetic steel. Measurements were taken in the horizontal and vertical directions, perpendicular to the rotor's axis of rotation. Fig. 16 shows a photograph of the turbogenerator with the accelerometers installed.

Fig. 16. Microturbine with uniaxial accelerometers installed on its casing in the vicinity of the bearing node

Selected measurement results obtained at different rotational speeds and microturbine power levels are presented as frequency distributions of vibration velocities in Figs. 17–19. The measurement results presented in this article are limited to vibrations recorded in the vertical direction. Vibrations in this direction were less affected by external influences and therefore better represented those of the microturbine itself. The frequency range was limited to 1,600 Hz, and the analysed parameter—vibration velocity—was expressed in mm/s.
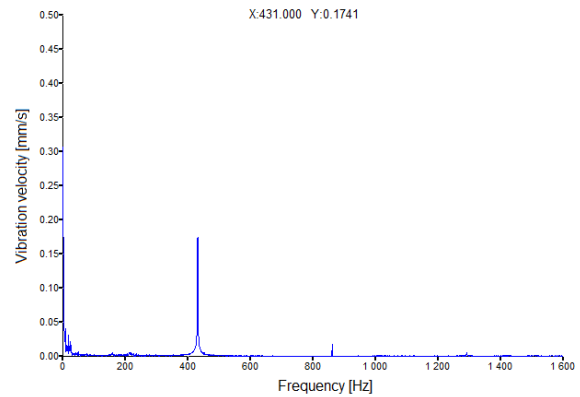

Fig. 17. Vibration velocity spectrum recorded on the microturbine casing in the vertical direction at a rotational speed of *25,860 rpm*
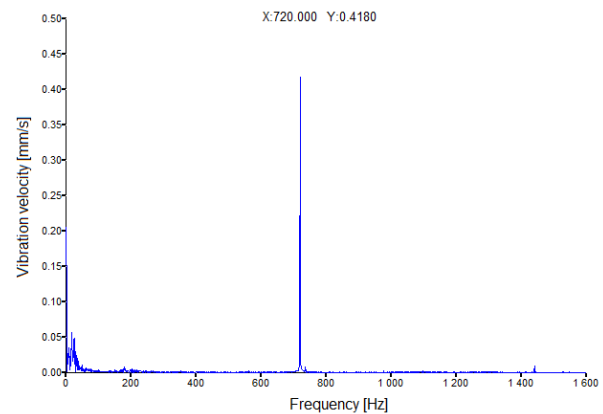

Fig. 18. Vibration velocity spectrum recorded on the microturbine casing in the vertical direction at a rotational speed of *43,200 rpm*
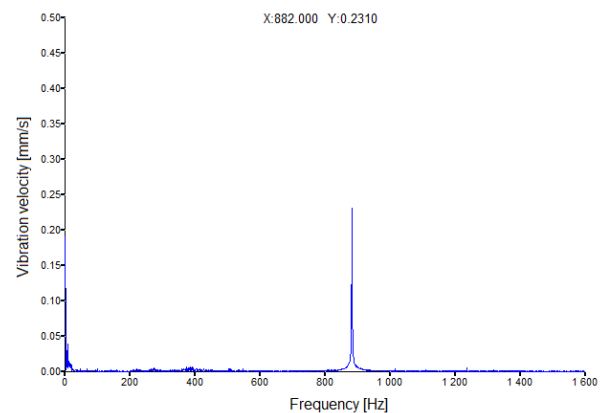

Fig. 19. Vibration velocity spectrum recorded on the microturbine casing in the vertical direction at a rotational speed of *52,920 rpm*

It was found that the level and distribution of the microturbine vibrations were not a cause for concern. The velocity amplitude of

the synchronous vibrations (with a frequency matching the rotor's rotational speed) reached a maximum of 0.418 mm/s at a rotor speed of 43,200 rpm. At higher and lower rotational speeds of the rotor, the vibration level was lower; for example, at 25,860 rpm, the velocity amplitude of the synchronous vibrations was 0.174 mm/s, and at 52,920 rpm, it was 0.231 mm/s. Apart from the synchronous component (the so-called 1x), only at certain speeds could a slight increase in vibration components at other frequencies be observed, as can be seen, for example, in Fig. 17, where the appearance of a superharmonic component (the so-called 2x) can be discerned.

In addition, an increased level of vibration at the lowest frequencies (below 100 Hz) can be observed in the characteristics shown above. However, these vibrations were not caused by the operation of the microturbine, but by the vibrations of the remaining subassemblies of the test rig and the movement of people in the laboratory.

Referring to the relevant standards for the measurement and evaluation of vibrations in rotating machinery, it was found that the dynamic condition of the ORC microturbine studied was very good. According to the ISO 20816-1 standard, the permissible level of the RMS value of the vibration velocity (Vrms) measured on the casing should not exceed 0.71 mm/s for new machines with capacities of up to 15 kW. In contrast, the permissible vibration velocity level for such machines, allowing long-term operation without any restrictions, is 1.8 mm/s. In the case of the microturbine tested, the specified vibration levels were not exceeded, regardless of the rotational speed or the thermal and electrical load. There were also no other vibroacoustic symptoms indicative of incorrect operation of the microturbine or any damage within the machine's rotating system.

4. CONCLUSIONS

Based on the research, it was determined, firstly, that irrespective of the heat source power, the electrical power output of the ORC system increased as the HFE-7100 medium flow rate increased. For heat source powers in the range of 12–20 kW_t and HFE-7100 flow rates in the range of 30–60 g/s, the optimum generator load at which the electrical power output of the ORC system was at its maximum lay in the range of 2.6–5.1 Ω.

Secondly, it was found that, irrespective of the heat source power, the isentropic efficiency of the microturbine decreased as the HFE-7100 flow rate increased. For heat source powers in the range of 12–20 kW_t and HFE-7100 flow rates between 30 and 60 g/s, the maximum isentropic efficiency of the microturbine lies between 50% and 70%, achieved with a load in the range of 3.5–10.5 Ω.

Thirdly, it was determined that the optimum load range for the microturbine generator, for a flow rate between 30 and 60 g/s and a heat source power between 12 and 20 kW_t, at which the Carnot efficiency was maximised, was from 2.1 Ω to 9.3 Ω.

Fourthly, it was found that, irrespective of the heat source power, the efficiency of the ORC system increased with increasing working medium flow rate. For a heat source power in the range of 12–20 kW_t and an HFE-7100 flow rate in the range of 30–60 g/s, the optimum generator load at which the ORC system efficiency reached its maximum lay in the range of 2.2–6.1 Ω.

Vibration measurements indicated that the microturbine operated correctly across the tested range of rotational speeds and under the preset thermal and electrical loads. The maximum vibration velocity recorded on the microturbine casing was 0.418 mm/s and occurred at 43,200 rpm. At other rotational speeds of the rotor, the level of synchronous vibrations was lower, and in none of the cases examined did the overall vibration level exceed the recommended values for new rotating machinery. This confirms that the developed ORC microturbine operated correctly under conditions typical of small cogeneration systems.

REFERENCES

1. Zhang Y, Tsai YCh, Ren X, Tuo Z, Wang W, Gong L, Hung TCh. Experimental study of the external load characteristics on a micro-scale organic Rankine cycle system. Energy. 2024:306;132453. https://doi.org/10.1016/j.energy.2024.132453

2. Zhang H-H, Zhang Y-F, Feng Y-Q, Chang J-Ch, Chang Ch-W, Xi H, Gong L, Hung T-Ch, Li M-J. The parametric analysis on the system behaviors with scroll expanders employed in the ORC system: An experimental comparison. Energy. 2023:268;126713. https://doi.org/10.1016/j.energy.2023.126713

3. Wei J, Hua Q, Yuan L, Li G, Wang J, Wang J. A review of the research status of scroll expander. Proceedings of the Institution of Mechanical Engineers, Part A: Journal of Power and Energy. 2023:237(1);176-197. https://doi:10.1177/09576509221109245

4. Kaczmarczyk TZ, Żywica G. Experimental research of a micropower volumetric expander for domestic applications at constant electrical load. Sustainable Energy Technologies and Assessments. 2022:49;101755. https://doi.org/10.1016/j.seta.2021.101755

5. Montazerinejad H, Eicker U. Recent development of heat and power generation using renewable fuels: A comprehensive review. Renewable and Sustainable Energy Reviews. 2022:165;112578. https://doi.org/10.1016/j.rser.2022.112578

6. Huo E, Xin L, Wang S. Thermal stability and pyrolysis mechanism of working fluids for organic Rankine cycle: A review. International Journal of Energy Research. 2022:46;19341–19356. https://doi.org/10.1002/er.8518

7. Wołowicz M, Kolasiński P, Badyda K. Modern Small and Microcogeneration Systems—A Review. Energies. 2021:14(3);785. https://doi.org/10.3390/en14030785

8. Alshammari F, Alshammari AS, Alzamil A. Advanced energy conversion strategies using multistage radial turbines in Organic Rankine Cycles for low-grade heat recovery. Case Studies in Thermal Engineering. 2025:69;106034. https://doi.org/10.1016/j.csite.2025.106034

9. Ahmed AM. Thermal efficiency investigation for organic Rankine cycle and trilateral flash cycle using hydrofluoroether working fluids. Results in Engineering. 2024:21;101648. https://doi.org/10.1016/j.rineng.2023.101648

10. Witanowski Ł. Multi-Objective Optimization of a Small-Scale ORC-VCC System Using Low-GWP Refrigerants. Energies. 2024:17(21);5381. https://doi.org/10.3390/en17215381

11. Hasan A, Mugdadi B, Al-Nimr MA, Tashtoush B. Direct and indirect utilization of thermal energy for cooling generation: A comparative analysis. Energy. 2022:238(Part C);122046. https://doi.org/10.1016/j.energy.2021.122046

12. Kaczmarczyk TZ. Experimental research of a pumping engine in a micro-ORC system with a low-boiling medium. Archives of Thermodynamics. 2024:45(4);125–140. https://doi.org/10.24425/ather.2024.152002

13. Zuo Q, Liu P, Meng W, Zeng X, Li H, Wang X, Tian H, Shu G. Bayesian

Tomasz Z. Kaczmarczyk, Grzegorz Żywica
Experimental Research of Thermal-Flow and Vibration Characteristics of a 1 Kw ORC Microturbine

DOI: 10.65731/ama/2026-0015

optimized LSTM-based Sensor Fault Diagnosis of Organic Rankine Cycle System. Energy and AI. 2025;100519. https://doi.org/10.1016/j.egyai.2025.100519

14. Li J, Gurgenci H, Guan Z, Li J, Li L, Xue Y. Multi-objective optimization of a small scale SCO_2 turbine rotor system with a shaft cooler. Mechanics & Industry. 2022:23;21. https://doi.org/10.1051/meca/2022018

15. Hossain MS, Sultan I, Phung T, Kumar A. An Optimum Design for a Fast-Response Solenoid Valve: Application to a Limaçon Gas Expander. Dynamics, 2024:4(2);457-474. https://doi.org/10.3390/dynamics4020024

16. Zaniewski D, Klimaszewski P, Klonowicz P, Witanowski Ł, Lampart P, Jędrzejewski Ł, Suchocki T. Organic Rankine cycle turbogenerator cooling – Optimization of the generator water jacket heat exchange surface. Applied Thermal Engineering. 2023:223;120041. https://doi.org/10.1016/j.applthermaleng.2023.120041

17. Kaczmarczyk TZ, Ihantowicz E, Żywica G, Kaniecki M. Experimental study of the prototype of a Roto-Jet pump for the domestic ORC power plant. Archives of Thermodynamics. 2019:40(3);83-108. https://doi.org/10.24425/ather.2019.129995

18. Sanaye S, Ghaffari A. Transient modeling and thermal analysis of an innovative dual-loop Rankine–organic Rankine heat recovery system integrated with a gas engine. Journal of Thermal Analysis and Calorimetry. 2023:148(20);10951-10971. https://doi.org/10.1007/s10973-023-12435-3

19. Murthy AA, Norris S, Subiantoro A. Performance of a four-intersecting-vane expander in a R134a refrigeration cycle. Applied Thermal Engineering. 2022:209;118244. https://doi.org/10.1016/j.applthermaleng.2022.118244

20. Peng N, Wang E, Wang W, Lu J, Li M. Aerodynamic analysis of a 1.5 kW two-stage counter-rotating partial-admission impulse turbine for small-scale power system with a high expansion pressure ratio. Case Studies in Thermal Engineering. 2024:53;103824. https://doi.org/10.1016/j.csite.2023.103824

21. Gunawan G, Permana DI, Soetikno P. Design and numerical simulation of radial inflow turbine of the regenerative Brayton cycle using supercritical carbon dioxide. Results in Engineering. 2023:17;100931. https://doi.org/10.1016/j.rineng.2023.100931

22. Zhang Y, Zhang S, Peng H, Tian Z, Gao W, Yang K. Thermodynamic analysis of Tesla turbine in Organic Rankine Cycle under two-phase flow conditions. Energy Conversion and Management. 2023:276;116477. https://doi.org/10.1016/j.enconman.2022.116477

23. Wang E, Peng N. A Review on the Preliminary Design of Axial and Radial Turbines for Small-Scale Organic Rankine Cycle. Energies. 2023:16(8);3423. https://doi.org/10.3390/en16083423

24. He S, Tong Z, Tong S, Chen K, Cao XE. Collaborative optimization of turbo-expander impellers and guide vanes to mitigate flow-induced vibrations. Physics of Fluids. 2025;37(3);035178. https://doi.org/10.1063/5.0257754

25. Ahmed AM. Assessment of the thermal efficiency of subcritical power generation cycles using environmentally friendly fluids at various heat source temperatures. Energy Sci. Eng. 2022:10;4768-4781. https://doi.org/10.1002/ese3.1307

26. Peng N, Wang E, Wang W. Design and analysis of a 1.5 kW single-stage partial-admission impulse turbine for low-grade energy utilization. Energy. 2023:268;126631. https://doi.org/10.1016/j.energy.2023.126631

27. Witanowski Ł, Klonowicz P, Lampart P, Ziółkowski P. Multi-objective optimization of the ORC axial turbine for a waste heat recovery system working in two modes: cogeneration and condensation. Energy. 2023:264;126187. https://doi.org/10.1016/j.energy.2022.126187

28. Kottapallia A, Konijeti R. Numerical and experimental investigation of nonlubricated air scroll expander derived from a refrigerant scroll compressor. Front Heat Mass Transfer. 2022:19(1);1-11. https://doi.org/10.5098/hmt.19.11

29. Daniarta S, Kolasiński P, Imre A.R, Sowa D. Artificial intelligence-driven performance mapping: A deep learning-based investigation of a multi-vane expander in retrofitted organic Rankine cycle. Energy Conversion and Management. 2024:315;118763. https://doi.org/10.1016/j.enconman.2024.118763

30. Colak AB, Arslan O. Numerical analysis-based performance assessment of the small-scale organic Rankine cycle turbine design for residential applications. Thermal Science and Engineering Progress. 2024:51;102626. https://doi.org/10.1016/j.tsep.2024.102626

31. Abdalhamid AMK, Eltaweel A. Design and analysis of a single-stage supersonic turbine with partial admission. Energy. 2024:309;133100. https://doi.org/10.1016/j.energy.2024.133100

32. Abbas WKA, Baumhögger E, Vrabec J. Experimental investigation of organic Rankine cycle performance using alkanes or hexamethyldisiloxane as a working fluid. Energy Conversion and Management: X. 2022:15;100244. https://doi.org/10.1016/j.ecmx.2022.100244

33. Sun H, Gao P, Wu X. Performance investigation of a two-stage partial admission axial impulse turbine used for low temperature organic rankine cycle. Renewable Energy. 2025;249:123276. https://doi.org/10.1016/j.renene.2025.123276

34. Kaczmarczyk TZ, Żywica G. Experimental study of the effect of load and rotational speed on the electrical power of a high-speed ORC microturbogenerator. Applied Thermal Engineering.2024:238;122012. https://doi.org/10.1016/j.applthermaleng.2023.122012

35. Sun H, Li H, Gao P, Hou F, Hung TCh, Chang YH, Lin ChW, Qin J. Numerical simulation and low speed experiment of a low partially admitted rate axial turbine for small scale organic Rankine cycle. Applied Thermal Engineering. 2024:238;122002. https://doi.org/10.1016/j.applthermaleng.2023.122002

Tomasz Z. Kaczmarczyk: https://orcid.org/0000-0003-4954-8002

Grzegorz Żywica: https://orcid.org/0000-0002-6848-5732